Model of impedance changes in unmyelinated nerve fibres

Ilya Tarotin*, Kirill Aristovich and David Holder

Abstract*— *Objective: **Currently there is no imaging method which is able to distinguish the functional activity inside nerves. Such a method would be essential for understanding peripheral nerve physiology and would allow precise neuromodulation of organs these nerves supply. Electrical Impedance Tomography (EIT) is a method which produces images of electrical impedance change (dZ) of an object by injecting alternating current and recording surface voltages. It has been shown to be able to image fast activity in the brain and large peripheral nerves. To image inside small autonomic nerves, mostly containing unmyelinated fibres, it is necessary to maximise SNR and optimize the EIT parameters. An accurate model of the nerve is required to identify these optimal parameters as well as to validate data obtained in the experiments. *Methods:* In this study, we developed two 3D models of unmyelinated fibres: Hodgkin-Huxley (HH) squid giant axon (single and multiple) and mammalian C-nociceptor. A coupling feedback system was incorporated into the models to simulate direct (DC) and alternating current (AC) application and simultaneously record external field during action potential propagation. *Results:* Parameters of the developed models were varied to study their influence on the recorded impedance changes; the optimal parameters were identified. The negative dZ was found to monotonically decrease with frequency for both HH and C fibre models, in accordance with the experimental data. *Conclusion and significance:* The accurate realistic model of unmyelinated nerve allows optimisation of EIT parameters and matches literature and experimental results.**

***Index Terms*—Bioimpedance, electrical impedance tomography (EIT), finite element method, nerve model.**

I. Introduction

ELECTRICAL impedance tomography (EIT) is a technique which allows imaging apparent impedance changes (dZ) of a body by applying alternating currents and recording voltages measured with surface electrodes. With EIT, it is possible to image slow dZ occurring due to blood flow changes or cell swelling [1] as well as fast changes during neural depolarization [2], [3], which is referred to as fast neural EIT.

There is currently no technique which allows non-invasive imaging of fascicular activity in peripheral nerves. Such a technique would be crucial in the understanding of normal and abnormal peripheral nerve activity. In addition, this will facilitate more precise real-time neuromodulation techniques, such as the emerging field of electroceuticals [4], which aims at selective stimulation of the fascicles supplying different organs and therefore for treating various associated illnesses.

Current potential methods include inverse source localization in EEG or MEG, usage of microelectrode arrays (MEAs) or optical methods, such as voltage-sensitive dyes together with confocal or two-photon microscopy techniques. However, they either have poor spatial resolution (EEG, MEG) [5], are invasive and alter peripheral nerve function and cause significant damage (MEAs) [6] or are expensive, have small fields of view (<1 mm^2) and therefore insufficient imaging volumes (<1 mm^3); they also require a high exposure which limits temporal resolution (optical methods) [7], [8].

Fast neural EIT has been successful in imaging electrically evoked fascicular activity of the largest myelinated fibres in rat sciatic nerve [9]. In order to extend fast neural EIT to work in small autonomic nerves containing mostly unmyelinated, slow-conducting fibres, with a smaller impedance response, EIT parameters have to be optimised. These parameters include optimal strength and frequency of injected current as well as electrodes position and geometry. Also, thorough validation of experimental recordings has to be performed in order to understand consequences of the underlying interaction between applied current and dynamic conduction of action potentials.

Currently, there is no model able to accurately and simultaneously simulate both intracellular and extracellular electric fields in 3D for interacting active fibres. Ideally, the model would contain thousands of closely packed active unmyelinated and myelinated interacting fibres with varied sizes, propagation velocities and ion channel properties. This paper addresses the gap by developing the first building block of such a complete model via introducing the unmyelinated fibres (HH fibres with three ion channels and realistic mammalian C fibres containing ten ion channels) with their accurately simulated external and internal electric fields. In addition, groups of 2, 4 and 8 fibres whose extracellular fields affect each other were modelled. Various parameters affecting these models were studied including electrodes position, injected current and fibre complexity. The resulting model enables the experimental data previously obtained for an unmyelinated crab leg nerve to be interpreted and give

This research was supported by GSK/Verily (Galvani Bioelectronics)-UCL collaboration grant "Imaging and selective stimulation of autonomic nerve traffic using Electrical Impedance Tomography and a non-penetrating nerve cuff".

*I. Tarotin, K. Aristovich and D. Holder are with the Department of Medical Physics and Bioengineering, University College London, London WC1E 6BT, U.K. (e-mail: ilya.tarotin.14@ucl.ac.uk; k.aristovich@ucl.ac.uk; d.holder@ucl.ac.uk).

preliminary values for optimal parameters of EIT.

The applications of the resulting full model are not limited only to optimizing EIT but also include an opportunity to study various nerve diseases, such as ones associated with demyelination, mechanical damage or subjection to different external stimuli.

A. *Fast neural electrical impedance tomography (EIT)*

The main principle of EIT is the injection of alternating current through a pair of electrodes with recording of the resulting voltages at the remaining electrodes. Several hundred measurements can be made by switching between injection electrode pairs [10]. With the use of numerical methods such as finite element method (FEM) and inverse problem techniques, tomographic images of the internal electrical impedance of the tissue can be reconstructed.

Fast impedance changes occur during neuronal depolarization and are generally decreases in resistance of about 0.1-1% with millisecond durations. Fast neural EIT has been shown to be successful in imaging fast neural activity of somatosensory cerebral cortex of the rat during evoked potentials with the use of 30 electrode surface epicortical arrays. The temporal and spatial resolution of the imaged changes were up to 2 ms and 200 μm respectively [11].

In addition, imaging in-vivo fascicle activity in a cross-section of a rat sciatic nerve during compound action potential (CAP) propagation was recently accomplished by our group. After electrical stimulation of associated distal branches, peroneal and tibial fascicles of the nerve were successfully visualized in 26 recordings in 4 rats [9]. Thus, EIT has been shown to be able to localize functional activity in peripheral nerves, which is a major milestone towards imaging in autonomic nerves.

There are several experimental studies published on measurement of fast impedance changes in unmyelinated nerves; these studies are suitable for comparison with the models being developed in the current study. The experimental design of the work done in our laboratory in crab walking leg nerve was similar to the one used in this paper [12]. It comprised 2 current injecting electrodes, 2 recording electrodes and 2 stimulation electrodes which triggered CAP propagation along the unmyelinated nerve. Measurements were undertaken in 12 crab walking leg nerves at 225, 625 and 1025 Hz, amplitudes of 5, 10 and 20 μA and 0, 20 and 40˚ phases with respect to stimulation pulse. Impedance changes (dZ) observed were decreases of up to 0.05% at 225 Hz decreasing with frequency to ~0.02% at 1025 Hz, which is consistent with earlier studies. Using a similar experimental paradigm, [2] measured dZ at 125 to 825 Hz on 15 crab nerves during AP propagation from 0.25 to 0.06%. In [13], in crab nerves, the change in dZ was about -0.7% at DC with no significant change at 50 kHz. Studies [14], [15] were alike: crab nerve impedance was found to decrease by around 1% at DC.

The classic explanation of the mechanism and physiological basis of fast neural EIT is based on a passive model of a neural membrane which is represented as a parallel connected resistance formed by ion channels and a capacitance produced by a lipid bilayer. When a neuron depolarizes, the ion channels that were previously closed - open, and the resistance decreases.AC current starts flowing through them causing a decrease in the bulk resistance of the tissue over milliseconds. Hence, qualitatively, the resistance of the depolarized neural tissue is expected to decrease while the extra ion channels remain open. Currents of higher frequencies can flow inside the neural tissue through capacitance in any state of ion channels, so the decrease of the impedance for higher frequencies will be lower with the highest value achieved at DC. Previous modelling of the nerve based on the passive cable model predicted this impedance-frequency dependence [16].

In contrast, the recently undertaken experiments have shown that the dependence of apparent impedance decrease on EIT current frequency is different from a simple decrease with frequency. These measurements differed from this model in two ways: i) The apparent impedance did not decrease to ~0 at frequencies higher than 1 kHz but was sustained at about -0.1% [17] and ii) An apparent impedance *increase* was measured [18]. A passive model cannot predict this behaviour.

The reason for this is that the real membrane is active where the value of the resistance depends on the voltage across it. In other words, ion channels are voltage-gated, so that they can interact with the alternating current injected during EIT. Thus, unlike the passive model where ion channels assume discrete open and closed states, the active membrane has a highly nonlinear resistance-voltage dependence that is influenced by applied currents of various frequencies.

B. *Membrane excitation and approaches to its simulation*

The cell membrane is the outer layer of the cell that contains a lipid bilayer and embedded proteins serving as diffusion barriers, known as ion channels. The main functions of the membrane are to protect the cell from the surrounding medium and to control the transport of ions through it into and out of the cell [19]. Neural cells can transmit information via electrical signals propagating along them. The action potential (AP) is the excitation wave moving along the excitable cell as the change in its membrane potential. APs are the basis of neural communication. They can propagate along axons to the axon terminals where they can be transmitted to other neurons through synaptic clefts. The physiological basis of the AP can be explained by the activity of voltage-gated ion channels in the membrane, where sodium and potassium channels play a pivotal role [20].

There are many neuronal models simulating excitation, which have been developed since the 1950s. The simplest model for simulation of the nerve tissue is the cable model with a resistance which can assume 2 states. It is based on cable theory; the membrane is represented as a constant resistance and a capacitance connected in parallel. Capacitance comes from the thin lipid bilayer which is able to store charge. The resistance representing ion channels is voltage-independent, and it takes on two fixed values when they are opened and closed. The resistance along the fibre is connected in series both inside and outside of the fibre. Such models have been developed by many researchers [21]–[23] as well as our group at UCL [16] but have not shown to be reliable enough to validate experimental data on impedance changes during AC application. This led us to consideration of models with active voltage-dependent resistance.

1) Hodgkin-Huxley (HH) model

The first and the most famous active model is the Hodgkin-Huxley (HH) model which simulates the electrical behaviour of the giant axon of the squid containing active sodium and potassium ion channels as well as a passive leakage channel [24]. The HH model represents the membrane as an electrical network with parallel-connected capacitance of lipid bilayer and the resistance of ion channels, which is variable and depends on the voltage across the membrane. The HH model is described by a system of differential equations, where the the coefficients were selected so that the response of the membrane to electrical stimulation was as close to experimental as possible. The currents through ion channels are controlled by so-called gating variables possessing values from 0 to 1; states of ion channels can continuously vary depending on the values of these variables. Propagation of action potentials initiated at a fixed point on the membrane can be described with the use of cable theory. The system of Hodgkin-Huxley equations can be extended by the inclusion of propagation terms taken from the cable equation:

$$\frac{r_{ax}}{2\rho_i}\frac{\partial^2 V_m}{\partial x^2} = C_m\frac{dV_m}{dt} + I_{Na}(V_m) + I_K(V_m) + I_{Leak}(V_m) \quad (1)$$

V_m and C_m are membrane potential, $[mV]$ and capacitance, $[\mu F/cm^2]$; r_{ax} is the radius of the axon, $[cm]$; ρ_i is the resistivity of the axoplasm, $[kOhm{\cdot}cm]$; I_{Na}, I_K and I_{Leak} denote sodium, potassium and leakage currents respectively, $[\mu A/cm^2]$; these currents are explained by a set of equations given in [24].

2) Complex active neural models

Since the basic Hodgkin-Huxley model is insufficient to describe all the observed behaviour accompanying excitation, new models of unmyelinated axons have been developed. They have been becoming more complicated by the addition of more ion channels and the tweaking of parameters so that they better correlate with the experimental data. These models steadily improved the accuracy of simulation of the action potentials' shape, excitability thresholds' temporal behaviour and its different complex features like activity-dependent slowing (ADS) and recovery cycles. For example, Scriven simulated repetitive firing phenomena by modelling the Na-K pump, finite intra-axonal and periaxonal volumes and calcium ion channels [25]; Herzog and colleagues first included TTX resistant sodium channels (now called $Na_v1.9$) in a model of DRG neurons [26]; Tigerholm together with his group were able to model activity-dependent slowing and recovery cycles for C-nociceptors [27]; Cross and Robertson studied ionic mechanisms accompanying high-frequency firing of the descending contralateral movement detector (DCMD) axons [28]. Numerous other neural models have been developed in recent years, including for myelinated fibres [29], [30] and for groups of fibres [31]–[33].

There are many types of ion channels present in nerve fibres of living organisms. Two basic channels (also the most widespread) which were included in the HH model are sodium (Na) and potassium (K) channels, responsible for generation and stabilization of an action potential respectively. The ion channels shown to be present in mammalian autonomic nerve [34]–[42] have been included in the model of unmyelinated fibre to be developed in this study. These comprise the sodium channels responsible for depolarization and subthreshold excitability, $Na_v1.7$, $Na_v1.8$ and $Na_v1.9$, potassium channels whose main function is to regulate the resting potential are K_{DR}, K_M, K_A, K_{Na}, hyperpolarization-activated HCN channels regulating repetitive firing and pace-making and the Na-K pump and passive leakage channels which also help to make the resting potential of the membrane to be stable.

C. Purpose

The overall purpose of the work presented in this paper was to develop models of single and multiple unmyelinated nerve fibres and evaluate how impedance changes across them during the action potential. This was evaluated in models of one, two, four and eight interacting squid giant axons with Hodgkin-Huxley ion channels and a single C fibre with human nociceptor ion channels. Specific questions to be addressed were:

1) How does the impedance change vary with experimental parameters? These include
   a) AC amplitude and frequency;
   b) size and position of the electrodes;
   c) number of fibres and interaction between them;
   d) model complexity;
2) Does this agree with the previous studies?
   a) Does the model confirm experimental recordings [2], [12]–[15]?
   b) Does it offer any explanation?
   c) Does it differ from the previous modelling [16]?
3) Which model options are recommended for further modelling studies?

The answers obtained will help us to proceed further towards the development of a whole nerve model.

II. Methods

A. Overview

The work was divided into the following steps:

1) A FEM Hodgkin-Huxley model of the squid giant axon was developed in three-dimensional space. An action potential was induced at the distal end of the axon and its propagation was simulated intra- and extracellularly. External ring electrodes were modelled to apply an electrical current (two electrodes) and to record the axonal activity (one electrode with respect to ground) (Fig. 1). The model was transformed into the equivalent 2D axisymmetric one to accelerate computations. The effects of varying experimental parameters on dZ were studied. This model became the basis for all further simulations.
2) Additional axons were added such that their extracellular action potentials influenced each other. The effects of increasing number of fibres and their interactions was studied with 2, 4 and 8-axonal nerves.
3) A full accurate 3D model of a C fibre (and corresponding 2D axisymmetric model) containing ten experimentally validated ion channels and variable concentrations of the present ions was developed using the space-clamped model of Tigerholm [27]. Same simulations as for the HH fibre were accomplished.

The C fibre model was compared with a spatially modified HH model: the model dimensions, fibre diameter and axoplasm resistivity were reduced to match the C fibre, while temporal properties matched those of the classic HH model. This was done to compare how the complexity of ion channels and spatial structure affects an impedance change.

4) The impedance changes simulated in the developed models were compared with the experimental data previously obtained on the unmyelinated crab nerves to verify its general agreement and to choose the model of unmyelinated axon for further inclusion in the full model of the nerve.

B. General modelling principles

A model comprising a simultaneous simulation of electrical fields generated by nerve fibres and external sources in intra- and extracellular spaces was constructed using the finite element method (FEM) approach in COMSOL Multiphysics software (COMSOL Inc, USA). The finite element method implies the decomposition of the model geometry into separate parts so that element equations approximating the original ones are locally solved in each of the parts. These equations are then assembled into the global domain and solved there using initial conditions [43]. With the use of FEM, COMSOL allows automating the solution of partial differential equations describing neural tissue in temporal and spatial dimensions.

A simplification of the experimental design [12] in the crab leg nerve with the 4-electrode impedance measurement paradigm was simulated. In this experiment, an excised crab nerve was placed on a linear electrode array, action potentials were stimulated by 2 electrodes at the proximal end of the nerve, current was injected in the middle and voltages were measured between the electrode situated before the injecting ones and the one at the distal end of the nerve.

The geometry of the model consisted of extracellular space represented by a 3D cylinder with the electrical conductivity of an extracellular medium equalling 10 *mS/cm* (Fig. 1a) [44]. Axons were represented as 1D lines, meaning that consideration of the membrane and intracellular space was not necessary. In the model, the full transfer impedance of the system "fibre+external space" (Z) was continuously measured; this impedance changed during AP propagation (dZ). By injecting current and measuring external voltage the dZ modulating this voltage could be measured. Equations representing Z and dZ in terms of injected current and measured voltage are presented below:

$$Z = \frac{V}{I} = \frac{|V|e^{j(\omega t+\varphi_V)}}{|I|e^{j(\omega t+\varphi_I)}} = |Z|e^{j(\varphi_V-\varphi_I)} \approx |Z| \qquad (2)$$

In the equation, *Z*, *V* and *I* are complex values representing electrical impedance of the system, measured voltage and injected current, $|Z|$, $|V|$ and $|I|$ are their amplitudes; φ_V and φ_I are voltage and current phases, where the phase shift $\Delta\varphi = \varphi_V - \varphi_I \approx 0$ as the membrane does not significantly change the phase of the externally measured current (Results, Fig. 10) [45]. However, the small phase shift may affect the measurements at high frequencies (Results, Fig. 6, Fig. 10).

$$dZ = \frac{Z(t)-Z(t_0)}{Z(t)} = \frac{|V(t)|e^{j\Delta\varphi}-|V(t_0)|e^{j\Delta\varphi_0}}{|V(t)|e^{j\Delta\varphi}} \approx \frac{|V(t)|-|V(t_0)|}{|V(t)|} = |dZ| \qquad (3)$$

Impedance change dZ is equal to the relative change of the impedance $Z(t_0)$ when AP passes under the electrodes with respect to the baseline impedance of the system $Z=Z(t)$. Using (2), the complex dZ and absolute $|dZ|$ can be expressed in terms of the measured voltages $V=V(t)$ and $V(t_0)$.

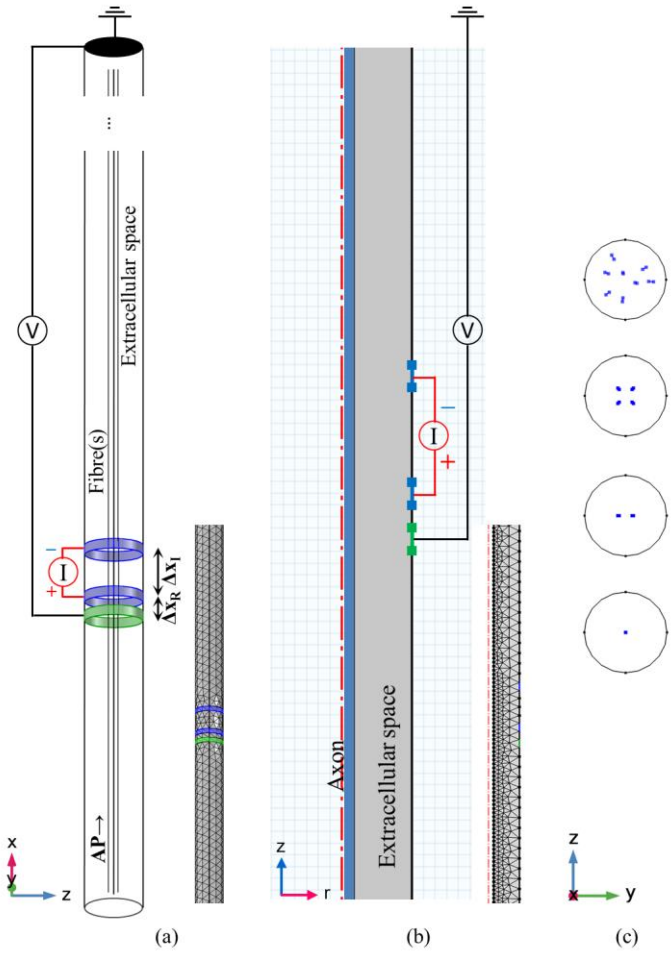

Fig. 1. (a) The 3D geometry of the models and corresponding 3D FEM mesh. AP was induced from the end of the axon(s); DC or AC was applied through two external electrodes (blue) placed approx. 18.75 cm from the axon's end (s.m. *B*); the electric field was recorded by an external electrode (green) placed before the injecting ones (with respect to ground). Detailed models' geometric dimensions are given in the s.m. *B* and *C*;
(b) Equivalent 2D axisymmetric model with a single fibre and corresponding triangular FEM mesh;
(c) Side view on the 1-, 2-, 4- and 8-axonal HH models. In the 8-axonal model, axons were randomly distributed inside the cylinder.

Application of alternating current was simulated via two ring extracellular electrodes situated on the boundary of the cylinder. Action potentials were initiated at the end of the axons by bipolar stimulation, either simultaneously or randomly to generate CAP. The compound activity was recorded by an equally sized electrode situated before the injecting ones with respect to ground. The model was grounded at the distal end only to prevent the current from propagating along the fibre in the direction opposite to the AP

and subsequently causing artefacts in dZ measurements [12].

The model was developed using the coupled feedback approach: the current injected through the external electrodes affected the fibres and the fibres' activity affected the external electric field recorded by the external electrode. The system of equations (4) - (6) describing the developed coupled feedback model is presented in the supplementary material, *part A*.

For an accurate simulation of the fibre and external volume conductor affecting each other, 1D and 3D problems corresponding to them had to be solved twice. Otherwise, the extracellular action potential modelled by coupling the transmembrane current from the fibre to the external space would be coupled back into the fibre. That would mean that the fibre would be doubly affected by its own electric field that is already implicitly included in the cable theory underlying AP propagation. Thus, the main 1D/3D pair (Fig. 2, top) served for simulation of the fibre, current injection into it and external activity recording. The additional 1D/3D pair (Fig. 2, bottom) did the same simulations but without injected current. The simulated external electric field in the adjoint 3D geometry (EAP with no current) was being subtracted from the compound activity in the first 3D geometry to be applied to the fibre at each simulation step ($V\text{-}V_1$ on the Fig. 2, s.m. Fig. 1).

A 3d tetrahedral mesh was constructed, and the fibres were divided at equal intervals so that they formed a continuous mesh within the volume. The length of these intervals and the size of the mesh elements close to the fibre depend on the model and must be much smaller for the C fibre than for the HH model. This is because the C fibre diameter is 10^3 times smaller, leading to the smaller space constant and associated AP characteristics. The number of elements also grows with additional fibres as many small elements appear between the adjacent fibres.

In the developed models, a constant resistance of the external space is known (*0.1 kΩ·cm,* s.m. *A*); the impedance of the fibre was variable and depended on the transmembrane voltage (1). A set of volume conduction equations (5)-(6) and axonal activity equations (8) or (10)-(26) (s.m. *A*) were solved for each time step simultaneously with respect to V_m and V_e using an adaptive backward differentiation formula (BDF) together with a parallel sparse direct solver (PARDISO) for handling corresponding linear equations. Using the same approach as in the experiment [12] and the voltages obtained by solving the above equations, changes in the impedance Z of the system "fibre + external space" (*dZ*) were measured employing the identical signal processing routine (*s.m. E*). We did not separately consider the membrane and the volume inside the fibre as we were interested in the electrical properties and corresponding impedance changes of the system as a whole.

To accelerate computations of single-fibre models without reducing their complexity, 3D models were transformed into the 2D model with axial symmetry (Fig. 1b). For this, spatial coordinates (*x, y, z*) were exchanged for the cylindrical ones (*r, z)*, the same was performed for the del operators in (2), (5), (6). Unlike in the 3D model with 1-dimensional fibre, in the 2D model the fibre was represented as a cylinder which did not significantly affect the precision of simulations at the distances exceeding fibre diameter (see Results, Fig. 4). The model had a triangular FEM mesh which made the computations up to 10 times faster. The main disadvantage of this model is its lack of flexibility: multiple fibres and non-symmetric electrodes cannot be simulated.

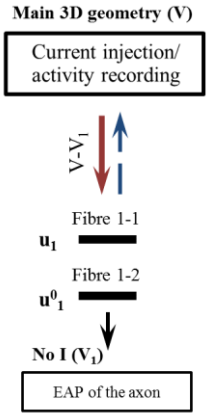

Fig. 2. Schematic representation of the feedback coupling models' operation for a single fibre. Additional 3D geometry was to simulate electric field of the "pure" EAP with no injected current (V_1); at each time step, their difference with the main field (V, with injected current) was applied to the active fibre ($V\text{-}V_1$, red line) and resultant membrane current was coupled to the main 3D geometry (blue dashed line).

C. FEM model of Hodgkin-Huxley squid giant axon

Geometrical parameters of the HH model were as follows: the axon was 60 cm long, the recording electrode was situated 18.65 cm from the AP initiation point; with the injecting electrodes placed 0.1 cm further, separated by a 0.4-cm gap. All the electrodes had a cylindrical shape, were 0.1 cm in width and 0.6 cm in diameter (Fig. 1a). The extracellular space had a cylindrical shape with the same diameter as the electrodes. The diameter of the squid giant axon was 0.1 cm, but it was modelled as a 1D line as the internal potential was not needed.

Additional parameters and initial values of the model are shown in supplementary material, *part B* (s.m. Table II).

The first step was to study the effect of reducing the model into the 2D axisymmetric paradigm. For that, impedance changes simulated with this model at DC and 625 Hz were compared with the ones obtained with the 3D model (Fig. 1a, b). Then, direct currents of various amplitudes (1.9 – 188 µA) and of two polarities at each amplitude were injected to check the amplitudes at which the impedance change was proportional to the applied current as it follows from Ohm's law. Too small currents would not allow dZ measurement due to modelling errors or, in case of experiments, due to instrumentation noise; too large currents would influence the ion channels and modify the nerve physiology so that the dZ recordings become unreliable. Thus, another challenge was to find the optimal AC amplitude for the nerve dZ recording. The chosen amplitude was used at all studied frequencies. The same procedure was performed using 625 Hz AC, with a larger range of currents (1.9 – 754 µA).

Direct current and a range of alternating currents at 225 Hz, 625 Hz, 1025 Hz, 2, 4, 6, 8 and 10 kHz at the previously chosen amplitude were applied through the external injecting electrodes (specific details on the injection paradigm and signal processing are in *s.m. E*). The AP was initiated, and the

signal was recorded via the external recording electrode with respect to ground. Simulations lasted 40 milliseconds to let the action potential, velocity of ~15 *m/s*, propagate to the end of the axon. The recording sampling rate was 100 kHz.

The obtained impedance changes (see *section F* and s.m., *E* for details on its extraction from the recorded voltages) were validated by injecting the current in different phase-antiphase pairs locked to the AP initiation. This procedure allowed elimination of artefacts occurring from the action potential and its possible coherence with the AC wave. A more detailed explanation on this is discussed in the signal processing section.

To study the influence of the size and location of the electrodes on the simulations, diameters of the electrodes (and corresponding surrounding volume) and their widths were varied from 0.05 to 1 cm and 0.02 to 0.4 cm respectively. The position of the recording electrode with respect to the injecting pair (distance Δx_R), was varied from 0.02 to 5.1 cm. The same was done for the relative positions of the injecting electrodes Δx_I, from 0.2 to 5.1 cm.

To study artefacts introduced by moving the recording electrode, dZ was measured and compared at different distances before/after the current injection site (Δx_R) were compared (Fig. 8), to match the experimental technique [12].

To see how temperature affects impedance changes, DC and AC currents, at 225, 625, 1025 Hz, 2, 4 kHz, were injected at 6.3 (original temperature), 11 and 21ºC. This study was necessary for valid comparison of the results of the HH model with the C fibre model and crab nerve experiments.

All the geometric parameters of the carried-out simulations are shown in Table I.

TABLE I
GEOMETRICAL PARAMETERS OF THE MODELS

Parameter	HH axon	C fibre
Length	60 cm	2 cm
Fibre diameter	1 mm	1 µm
Propagation velocity	15 m/s	0.8 m/s
Diameter of the electrodes / surrounding volume, D_{el}	0.05 – 1 cm	5 – 100 µm
Width of the electrodes, H_{el}	0.02 – 0.4 cm	5 – 50 µm
Distance between recording and injecting electrodes, Δx_R	0.02 – 5.1 cm	10^{-3} – 0.1 cm
Distance between injecting electrodes, Δx_I	0.2 – 5.1 cm	10^{-3} – 0.1 cm

Finally, the changes in the flow of injected current through the membrane channels were studied to gain insight into the source of the observed apparent dZ. These changes were recorded and averaged at 18.65-18.75 cm, the same location as the recording electrode.

D. A multiple fibre model with/without interaction

A model with multiple interacting fibres contained adjacent HH axons forming an "artificial nerve", so that axons interacted via extracellular potentials. The interaction between adjacent fibres was included in the model, as it has previously been shown to affect each other's membrane potentials [46], [47]. It was assumed to be especially strong in the HH case because their extracellular APs have high amplitudes of about 6.5 mV (Fig. 3). The principles of operation of the models with multiple fibres are explained in the supplementary material, *part D* (s.m. Fig. 1).

In order to measure the effect of the number of axons on the impedance change and to study the effect of interaction, the same simulations as for a single HH axon, described in the previous section, were undertaken for 2, 4, and 8 interacting axons (Fig. 1c) – larger amount of fibres demanded considerably longer computation times.

E. Model of a realistic mammalian C fibre

Because the electrical properties of a giant axon in the HH model differ from those small unmyelinated fibres, and because it, therefore, could not predict the behaviour of their activity with high accuracy, a new complex model had to be developed. It was based on one of the latest experimentally validated models of unmyelinated fibres [27] where the temporal dynamics of ion channels in mammalian C-nociceptor had been simulated. Compared to this model, the one developed in this work additionally contained the spatial dimension to simulate AP propagation as well as coupling with the extracellular space to inject current and record the activity externally.

Compared to the HH axon, the dimensions generally decreased because the diameter, magnitude of EAP and propagation velocity of a C fibre were many times smaller (1 µm, 2 mV and ~0.8 m/s). Therefore, the diameter (and corresponding external volume) and length of the electrodes was reduced to 10 µm, and the length of the axon to 2 cm. The electrodes were situated 0.769 cm from the left end and the distances between them were: Δx_R = 0.01 cm and Δx_I = 0.002 cm (Fig. 1). This model was also constructed in a 2D axisymmetric paradigm, as was done for a single HH fibre. Its triangular mesh contained about 4800 elements with the fibre divided by 1600 intervals. The same simulations were carried out as for the HH axon, except the model variables were decreased. The range of measuring currents was 0.03 to 63 nA (0.02 – 40 mA/cm^2); distance from the recording electrode to the site of injection (Δx_R) and distance between the injecting electrodes (Δx_I) were varied from 10^{-3} to 0.1 cm; diameter and width of the electrodes were varied from $5{\cdot}10^{-4}$ to $1{\cdot}10^{-2}$ and $5{\cdot}10^{-3}$ cm respectively. Impedance changes at different recording positions were studied. Temperatures at which simulations were run included 37 (original temperature), 30 and 21ºC; frequency sweep was conducted at 21ºC for comparison with the HH axon. Additional detailed information on the model can be found in the supplementary material, *part C*.

To compare the effect of complex ion channels and spatial structure of the fibre on the impedance response, a simpler model able to represent the activity of small unmyelinated fibre, and with reduced computational demands, was developed: it had HH ion channels, but the diameter of the fibre was reduced, changing the action potential shape and propagation velocity. If the impedance response of this model matches the C fibre model, it will reduce complexity and aid in the development of the full model containing numerous axons. The geometric dimensions of the model were the same as in the C fibre model (s.m. part C); the diameter of the axon and the axoplasm resistivity were decreased to correspond to the C fibre (1 μm and 0.0354 $kOhm{\cdot}cm$). For this model, the

frequency sweep was carried out with the same parameters as for the C fibre and the processed data was compared to both previous models.

F. Signal processing

Signal processing to extract apparent impedance changes (dZ) was identical for all the constructed models and is presented in the supplementary material, *part E* (s.m. Fig. 2).

III. Results

A. 3D FEM model of a single Hodgkin-Huxley squid giant axon

In the model, the AP amplitude, duration, spatial length and propagation velocity (110 *mV*, 17 *ms*, 26 *cm*, 15 *m/s*) corresponded to those recorded experimentally by Hodgkin and Huxley [24]. The amplitude of the simulated extracellular AP was approximately 7 *mV* (Fig. 3a).

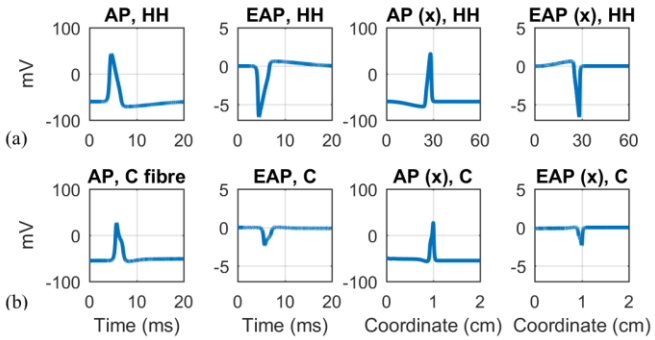

Fig. 3. Action potentials simulated with the developed models. (a) Hodgkin-Huxley model; (b) C fibre model. For both models, the first two columns show intracellular (AP) and extracellular action potentials (EAP) in time; columns 3 and 4 – along the fibre length.

In a 2D axisymmetric model, the impedance changes appeared to be close to the 3D model ones (for example, dZ at DC and 625 Hz are shown in Fig. 4a). The 2D axisymmetric model was then therefore used for all further single fibre simulations.

The modelled impedance changes were linear with the applied DC currents from 1.9 up to 7.5 µA (10–40 µA/cm^2). Currents in this range did not induce membrane excitation and the dZ values in percentage terms were equal for any of them (Fig. 5a). At higher currents, the dZ became nonlinear and started to depend on polarity. The upper limit increased at higher frequencies: for example, at 625 Hz dZ was still linear with the current at 377 µA (Fig. 5b). Thus, currents below 7.5 µA were "safe" at all frequencies so that they did not induce membrane excitation and the impedance changes were linear; 7.5 µA was therefore chosen for use in all simulations with HH axons.

For the initial geometry of the model (Fig. 1), the simulated negative apparent impedance changes fell with frequency from -3.36±0.04% at DC to -0.7±0.6% at 225 Hz, -0.8±0.2% at 625 Hz to -0.30±0.04% at 1025 Hz and were around zero above 2 kHz (Fig. 6a). The errors were larger at low frequencies because they were close to the characteristic frequency of impedance change (~200 Hz, Fig. 5a, b) resulting in errors in demodulation of corresponding sine waves (s.m. Fig. 2).

Significant dZ increases were observed at DC – 0.14±0.04%, and at high frequencies, where it was relatively constant at 2, 4 and 6 kHz: 0.06±0.04%, 0.07±0.02%, 0.06±0.01%, and decreased to 0.05±0.01% and 0.03±0.01% at 8 and 10 kHz (Fig. 6a). When increasing distances between the recording and injecting electrodes (Δx_R) and between the injecting electrodes (Δx_I), a dZ decrease was observed which was steeper with Δx_R (Fig. 7a).

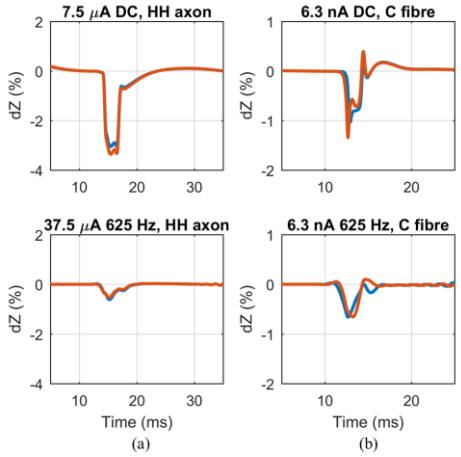

Fig. 4. Comparison of dZ computed with 3D (blue lines) and 2D axisymmetric (red lines) models of (a) a single HH axon and (b) a C fibre at DC (top) and 625 Hz (bottom). Time markers during simulation: AP excitation – 2 ms from the start (both fibres); AP passes under the recording electrode – 14.5 ms (HH axon) and 12 ms (C fibre), AP reaches the end of the fibres in 40 ms (HH axon) and in 26 ms (C fibre).

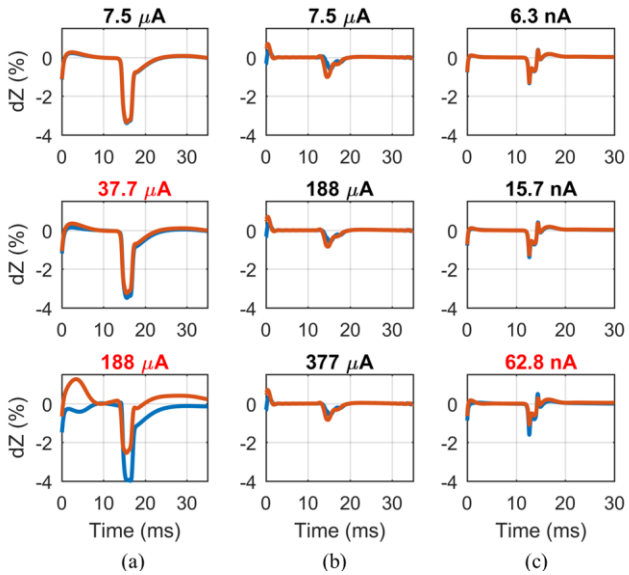

Fig. 5. Modelled impedance changes at various current amplitudes. Titles highlighted in red show the current outside the safe range. Red and blue lines designate dZ recorded with current at different polarities. Distortions at the starts of the dZ curves are edge effects caused by switching the current on and its effect on the membrane. Time markers are in the caption of Fig. 4.
(a) HH fibre, DC; (b) HH fibre, 625 Hz; (c) C fibre, DC.

There was also a decrease at very small distances determined by limitations of the model: the size of the mesh elements became larger than these distances. The maximum simulated values of dZ were at Δx_R = 0.1 cm and Δx_I = 0.35 cm. The impedance increase was constant along the range of these values. The negative and positive dZ decreased significantly with increasing radii of the electrodes and was approximately independent of their length (Fig. 7c).

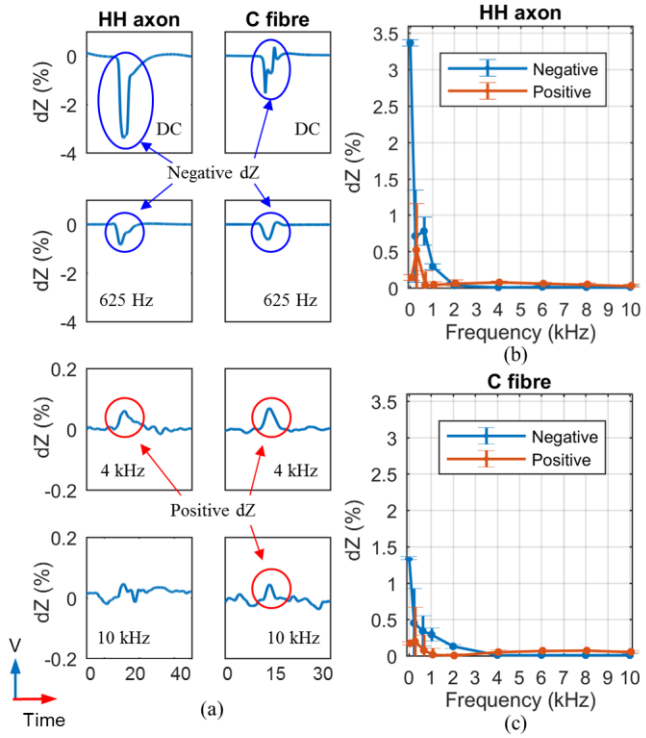

Fig. 6. (a) Examples of impedance changes (dZ) at DC, 625 Hz, 4 and 10 kHz. Negative impedance changes are highlighted by blues circles, positive ones – by red circles; (b) Absolute dZ vs. frequency for HH axon, I = 7.5 μA; (c) Absolute dZ vs. frequency for C fibre, I = 6.3 nA. Blue lines designate impedance decrease (negative change), red – impedance increase (positive change). Error bars are standard deviations calculated for the dZ simulated at different phases of the current (AC) and at different polarities (DC). Time markers are in the caption of Fig. 4.

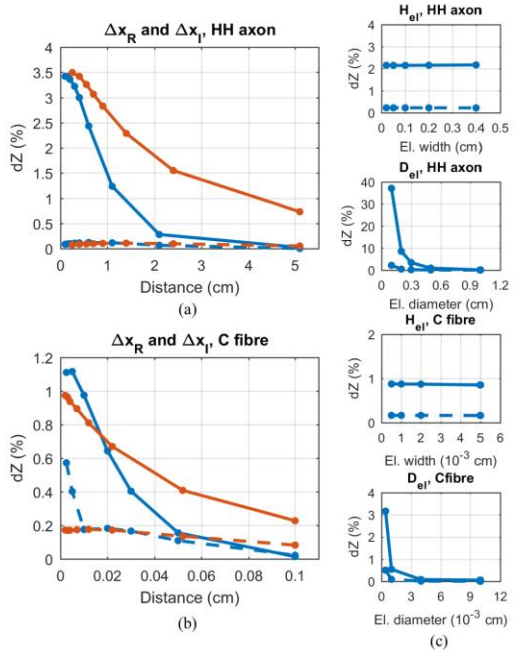

Fig. 7. Absolute impedance changes vs size and position of electrodes.
(a) HH model and (b) C fibre model dependence on distance between the recording and injection electrodes (Δx_R) and between injecting electrodes (Δx_I). dZ vs Δx_R is depicted with blue lines, dZ vs Δx_I – with red lines. Negative dZ are shown by full lines, positive – by dashed lines.
(c) Dependence of dZ on width (H_{el}) and diameter (D_{el}) of the used electrodes. HH model is on the top two graphs, C fibre – bottom graphs. Same as before, negative dZ are shown by full lines, positive – by dashed lines.

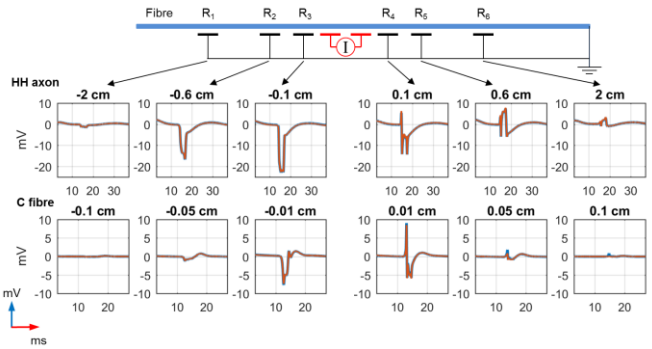

Fig. 8. Impedance changes simulated at DC with different positions of the recording electrode: 2, 0.6 and 0.1 cm before and after the site of injection. The dZ recorded prior the site of injection shape stays the same with magnitude falling with distance (left side). Artefacts appear after the site of injection, in accordance with [12] (right side). Colours represent different DC polarity.

The shape and negative polarity of the impedance change recorded before the site of injection was the same irrespective of the distance from it and the polarity of the current (Fig. 8). In contrast, the dZ measured with the electrodes placed after the injection site were affected by artefacts, in accordance with experiments [12].

As temperature increased, action potentials' durations and amplitudes decreased, and propagation velocities increased; however, the general behaviour of the dZ with frequency did not significantly differ across temperatures (Fig. 9a). The only feature found to depend on temperature was a steepness of decrease in the negative dZ with frequency. For instance, dZ decrease was zero above 625 Hz at 21ºC, while at the original temperature, it approached zero only at 2 kHz (Fig. 9a).

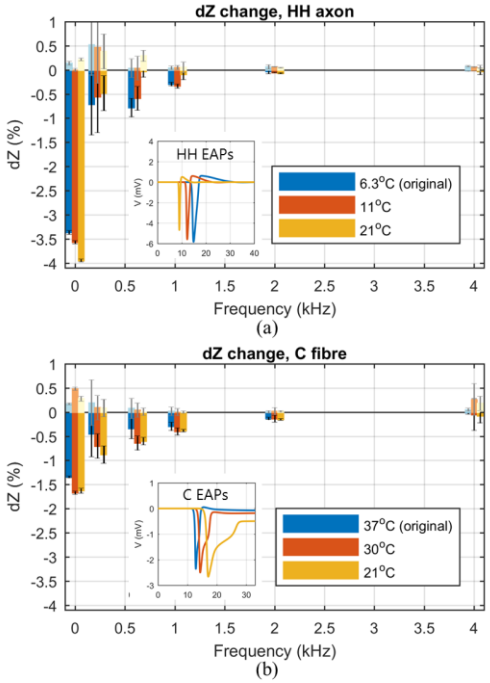

Fig. 9. Temperature dependence of the negative and positive impedance changes in the HH model (a) and the C fibre model (b). For the HH model, dZ were simulated at 6.3 (original temperature), 11 and 21ºC; for the C fibre: at 37 (original temperature), 30 and 21ºC. EAPs recorded at the same temperatures are embedded into the graphs.

Absolute changes in the EIT current flow through all the

pathways of the membrane were found during AP propagation at DC, at 625 Hz and at 4 kHz (Fig. 10b). At 625 Hz, before depolarization had reached the location of current injection (< 12 *ms*), there was a steady baseline current flow through capacitance (~2.2 $\mu A/cm^2$) and small flows through Na, K and leakage ion channels (~0.3 $\mu A/cm^2$ in total). During AP, there was a switch in the membrane path through which AC flowed: C-current fell significantly (to ~0.4 $\mu A/cm^2$) which was accompanied by increases in flows through ion channels to ~3 $\mu A/cm^2$. Total AC flow through the membrane also increased during AP from 2.4 to 3.5 $\mu A/cm^2$, equalling 45 % increase. This total increase in the current flow through the membrane explains the observed negative impedance change.

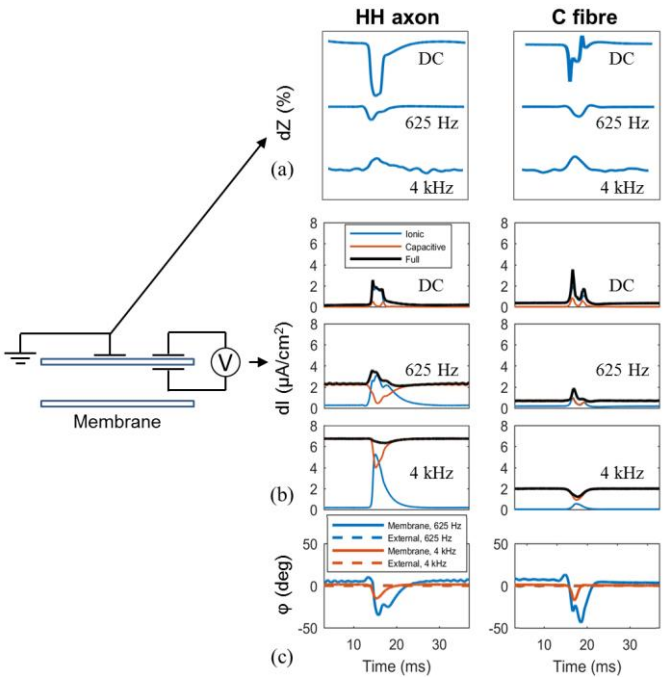

Fig. 10. Impedance changes, the associated change in the flow of the injected EIT current through the membrane and the change in its phase during depolarization. (a) Impedance changes at DC, 625 Hz and 4 kHz; this schematic picture repeats the one in Fig. 6; (b) Flow of the injected EIT current through ion channels (blue lines), capacitance (red lines) and full current flow (black lines) at DC, 625 Hz and 4 kHz for HH axon and C fibre; (c) Change in the phase of the injected AC current measured internally (i.e. current which has gone through the membrane, full lines) and externally (by the recording electrode, dashed lines) at 625 Hz (blue) and 4 kHz (red) for HH axon and C fibre.

At DC, there was no flow through capacitance at rest, consequently, there was a larger relative increase in the full current flow determining larger dZ (0.2 to 1.8 $\mu A/cm^2$, or 800 %) (Fig. 10b). At 4 kHz the behaviour of the currents flow was similar to 625 Hz. However, there was a small decrease in the total AC flow through the membrane (6.7 to 6.3 $\mu A/cm^2$, or 6%, Fig. 10b), which was due to a phase change of the current flowing through the membrane during depolarization (Fig. 10c). Because of this phase change, the absolute value of the total current change was not equal to the sum of the absolute values of changes of separate currents; therefore, a decrease in the current flow and an increase in the impedance could be seen (Fig. 6, Fig. 10). The phase change of the external signal recorded by the recording electrode was negligible (Fig. 10c) due to high baseline voltage (in accordance with the experimental study [45]); it did not allow to account for it in the dZ signal processing (Fig. 3).

B. Multiple fibre model. Effect of size and interaction

For increased axon numbers up to 8, the relationship between the number of axons and impedance change was close to linear, so that the ratio of dZ with N axons to dZ with 1 axon was close to N (Fig. 11). Also, the dZ response did not differ after turning off interaction between axons: one-way ANOVA test was accomplished which revealed no significant differences across multi-axonal models with and without interaction at all frequencies.

C. Complex mammalian C fibre model

Compared to the APs of HH axons, the action potential of a C fibre is shorter in duration and of a more complex shape, representing different properties of excitation such as depolarizing afterpotentials (DAP), hyperpolarizing afterpotentials (AHP) and others, as discussed in the introduction (Fig. 3b).

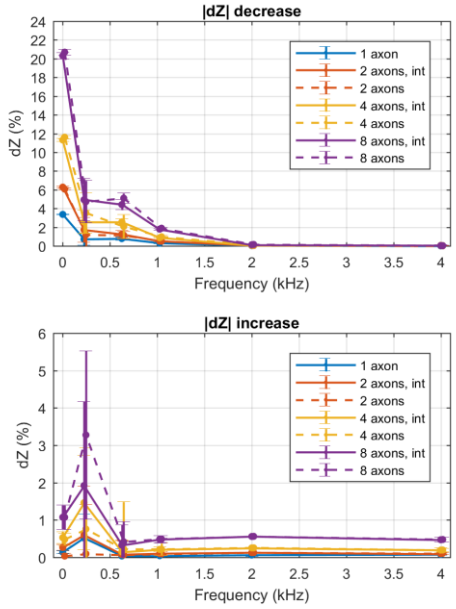

Fig. 11. Negative and positive impedance changes for 1-, 2-, 4- and 8-axonal HH models with and without interaction. Colours represent a model with a different number of axons. Models simulated with the interaction between axons are designated by full lines, without interaction – by dashed lines.

As for the HH axon, the difference in dZ of 3D and 2D axisymmetric models was indistinguishable (Fig. 4b).

The linear dependence of the C fibre dZ on the measuring currents from 0.6 to 6.3 nA (0.4 to 4 mA/cm^2) could be seen so that the percentage dZ change stayed the same at these currents (Fig. 5c). At 62.8 nA dZ became nonlinear and dependent on the polarity. Thus, 6.3 nA was shown to be the maximum current giving correct dZ values; it was therefore confirmed to be within the safe range and suitable for all further modelling.

The impedance response of a C fibre differed from the HH axon. The impedance changes were: -1.34 ± 0.02%, -0.45 ± 0.45%, -0.34 ± 0.21 %, -0.29 ± 0.09%, -0.13 ± 0.03% at DC, 225, 625, 1025 and 2000 Hz respectively; it was zero at higher frequencies (Fig. 6b). The positive impedance changes

comparable to those of the HH fibre were also recorded. They were significantly different from zero at DC, 4, 6, 8 and 10 kHz, with the values of 0.17±0.02%, 0.05±0.03% at DC and 4 kHz and 0.07±0.01% at 6, 8 and 10 kHz (Fig. 6b).

Apparent positive impedance changes appeared for the same reasons as for the squid giant axon, where the phase of the current flowing through the membrane changes during an AP.. This makes the absolute value of the sum of these currents different from the sum of their absolute values, causing an artefactual reproducible decrease in the total current flow and corresponding increase in the dZ (Fig. 10).

Large standard errors at low frequencies demonstrated high sensitivity of impedance changes to the phase of the applied current. The reason was that the characteristic frequency of the C fibre's dZ (~ 500 Hz, higher than of HH axon, Fig. 5c) was close to these frequencies affecting the precision of demodulation in signal processing (Fig. 3).

The negative impedance change decreased with increasing Δx_R and Δx_I, and the positive change stayed approximately constant, the same way as in HH fibre (Fig. 7b). High positive dZ was seen at very close distances to the site of injection (Δx_R < 0.01 cm), which could be due to edge effects of the current distribution. The recorded impedance change decreased with increasing electrodes diameter and did not change with their width (Fig. 7c). Equivalently to the HH case, the dZ artefacts appear only if the recording takes place after the site of current injection, in agreement with [12] (Fig. 8).

Frequency responses of the dZ at different temperatures did not significantly differ (Fig. 9b), the same as for the HH model. For this model, steepness of the dZ-frequency curve was found to be independent of temperature.

The impedance response for the model of a spatially modified HH axon which had the same geometric dimensions as in the C fibre model (including the size of the electrodes and the volume conductor, see *Methods*, *E* and *s.m.*, *C*), was close to that of the squid giant axon, even though the axon was 10^3 times smaller. The negative dZ fell about 8-fold from DC to 1 kHz, its values were: -2.28 ± 0.03%, -0.6 ± 0.6%, -0.57 ± 0.59%, -0.30 ± 0.08%, -0.17 ± 0.05% at DC, 225, 625, 1025 and 2000 Hz respectively and zero at other frequencies. Non-zero impedance increases equalling 0.08 ± 0.04% and 0.13 ± 0.05% were also observed at 4 and 6 kHz.

D. Comparison with experimental data

The negative impedance change values obtained in the crab nerve experiments (4–6ºC) at 125-1025 Hz [2], [12] together with those at DC [13]–[15] have the same frequency dependence as the ones simulated in this paper with all models. For example, in [2] authors obtained 0.25 to 0.06% negative changes at 125 to 825 Hz recorded on 15 nerves; in [12] negative dZ were from 0.05 to 0.02% at 225 to 1025 Hz respectively on 12 crab walking leg nerves. At DC, dZ equalling from 0.2 – 1 % were obtained [13]–[15]. No studies are available to confirm positive changes at high frequencies, – they are to be carried out in future.

The dependence of dZ on the distance between electrodes (Δx_R, Δx_I) predicted by the models developed here agreed with the experimental values for Δx_I [2], [14], [15] but differed from the ones for Δx_R [13], [15]. In the latter studies, authors claimed that Δx_R should be not less than 2 space constants so that the applied current does not modify it. However, simulations in the current study showed the converse – as long as the current is small enough, the AP is not modified by it even at the small distances from the site of injection (Fig. 8).

IV. Discussion

A. Summary of results

1) For both the HH and C fibre models and in keeping with experimental results [2], [12]–[15], a negative apparent impedance change was calculated which was maximal at DC and steadily decreased at higher frequencies (Fig. 6). The rate of the decrease was lower in the C fibre model which could be explained by complex ion channels kinetics and not the spatial properties of the model. In addition, in both models, this rate was lower than the one predicted by the previously developed Liston's passive model where no change is expected at above 1 kHz [16]. Small positive dZ were also observed at high frequencies and DC (Fig. 6).

2) The impedance changes did not depend on the amplitude of applied current in the safe range, the upper border of which equalled 7.5 µA for HH axon and 6.3 nA for a C fibre.

3) In a 3D model with multiple interacting axons, the dZ increase with the number of fibres was near-linear at all frequencies. The interaction between fibres did not significantly affect the simulated dZ (Fig. 11).

4) dZ generally decreased with increasing distances between the recording and injecting electrodes (Δx_R) and between injecting electrodes (Δx_I,). It corresponded to the experimental values for Δx_I [2], [14], [15] but differed from the ones for Δx_R [13], [15] where it was claimed that it had to be higher than two space constants not to modify the AP. However, modelling showed that AP is not modified at much closer distances if the electrode lies before the site of injection (Fig. 8). The impedance change decreased significantly with increasing electrode diameter and almost no change with increasing electrodes length (Fig. 7).

5) The absolute magnitude of impedance changes did not significantly differ with temperature in either model; steepness of decrease of the negative dZ with frequency increased with temperature for the HH model (Fig. 9).

6) The source of the apparent dZ during depolarization was due to an increase in total current through the membrane which, in turn, was caused by an increase in current flow through Na and subsequent increase through K ion channels. A small impedance increase can be explained by the inactivation phase of sodium channels at DC and by an AC phase change during AP at high frequencies (Fig. 10).

7) HH and C fibre models confirmed previous experimental findings: the highest negative impedance change was observed at DC and decreased with frequency in both models. The models also confirmed that to measure maximal dZ, the injecting electrodes should be as close as possible. However, contrary to the previous studies, findings suggest reduction of the distance between the recording and injecting electrodes: if the current is low enough, it will neither modify the AP nor cause an artefact (Fig. 8).

B. Answers to the stated questions

1) How does the impedance change vary with experimental parameters?

a) AC amplitude and frequency;

The maximum current level for the HH axon at which dZ were linear was 7.5 μA at DC (Fig. 5a); although slightly higher currents did not induce action potential, the impedance response became nonlinear and started to depend on the direction of the current, which is not suitable for experimental measurements. The safe range significantly widened with frequency (Fig. 5b). For a C fibre, the safe limit of the current not affecting the fibre was much smaller – 6.3 nA (Fig. 5c). Such a small current could be explained by very small electrodes needed to maintain a high current density.

The HH axon model with the initial electrode position has shown that the maximum dZ decrease was observed at DC and decreased with frequency, so that it was about 10 times smaller at 1025 Hz and approached zero at 4 kHz and above (Fig. 6). Small significant impedance increases were also observed at DC and higher than 4 kHz. The complex mammalian C fibre model also showed a similar dZ behaviour with the negative dZ decreasing with frequency; however, the steepness of this decrease was slower – about 2 times from DC to 1025 Hz compared to the 10 times for HH model and 8 times for spatially modified HH model (Fig. 6). Impedance increases with the same dependence on frequency were also observed.

b) size and position of the electrodes;

Electrodes location plays a vital role in the determination of the impedance change. For both models, negative dZ decreased with increasing Δx_R and Δx_I (Fig. 7a, b). Positive dZ were approximately constant across frequencies except for the C fibre one becoming artefactual at very small Δx_R. For both models, the dZ decreased with increasing electrodes diameter and stayed constant with increasing width (Fig. 7c).

c) number of fibres and interaction between them

The developed HH model with up to 8 axons demonstrated that the number of fibres had no effect on the impedance-frequency dependence and influenced only the magnitude of the impedance changes. Simulations showed that the approximate value of impedance change with increased axon number is equal to a single-axon dZ multiplied by a number of axons (Fig. 11).

With one-way ANOVA test, the interaction between fibres was shown not to be critical for evaluating the absolute dZ in the HH model. It did not affect the general trend of the impedance-frequency response and its effect did not rise with the number of fibres (Fig. 11).

For a C fibre model, the magnitude of its EAP on the surface is 3 times smaller than the one of the HH axon (Fig. 3) meaning that the effect on the adjacent fibres will also be considerably smaller even if they are closely packed. Thus, the interaction can be assumed to have no significance for dZ simulation in this model as well.

d) Model complexity

The complexity of the model significantly affected magnitudes of simulated dZ but did not influence its overall behaviour with frequency. The slope of the dZ decrease of the complex fibre was smaller compared to the HH axon as well as the modified HH axon with the reduced size. Therefore, it can be inferred that the kinetics of complex ion channels play a key role in determination. In addition, when the two models were simulated at the same temperature (21ºC), the slopes remained at similar levels.

2) Does this agree with previous studies?

a) Does the model confirm the experimental recordings?

A described behaviour of the impedance decrease with frequency is in agreement with the obtained experimental data for the unmyelinated crab nerve [2], [12]–[15].

Absolute values obtained for the whole thousands-of-fibres crab nerve were not many times higher than the ones modelled here due to several reasons. First, fibres in the real nerve do not fire simultaneously which causes dispersion weakening the compound action potential formed by APs of separate fibres; that consequently decreases the amplitude of the impedance change. Also, to obtain visible impedance changes of a single fibre, the modelled electrodes were 1) extremely small ($1.6 \cdot 10^{-4}$ mm^2 surface for a C fibre) to inject low current with a high current density; 2) located very close to the fibre ($5 \cdot 10^{-3}$ mm) to increase the amplitude of the recorded EAP. It strongly increased the obtained absolute dZ compared to the experimental ones where the surface of the smallest used electrodes was up to 0.5 mm^2 [12]. Finally, there was plenty of connective tissue with conductivity lower than extracellular fluid modelled in this study.

However, the model reached its original purpose which was to validate general dZ behaviour with EIT parameters, find the optimal parameters to obtain the largest response and to investigate into a biophysical explanation of impedance changes. Also, because the dependence of the negative dZ on frequency did not change with the number of fibres, predictions on frequency obtained for a single fibre can be used for a real nerve experiments which is a significant result of the current work.

b) Does it offer a biophysical explanation?

The analysis of the membrane currents in both models has shown that the nature of the externally recorded apparent impedance change could be presented as a superposition of two effects: change in the current amplitude flowing through different membrane channels and change of its phase accompanying excitation.

The significant apparent positive impedance changes were simulated at DC and at high frequencies. The ones at DC appear straight after the negative change and were due to the inactivation phase of the sodium ion channels (a small decrease in the full current flow in respect to the resting state follows depolarization at DC, Fig. 10b); they become negligible for AC. These changes show the real increase in the membrane impedance because the resistance of the membrane during ion channels inactivation decreases compared to the resting state.

The apparent positive dZ at high frequencies were found to be associated with the change in the phase of the injected current flowing through the membrane (Fig. 10). AC phase alters during AP at all frequencies, but due to the same time of occurrence with the negative change and because the negative change is much larger, significant positive dZ related to a phase change can be observed only at high frequencies where

negative changes are absent. These changes do not reflect the rise of real membrane impedance consisting of the active (resistive) and reactive (capacitive) components; conversely, they show an artefactual dZ increase appearing due to the summation of sine waves in divergent phases corresponding to the flow of AC current through ion channels and capacitance.

Although the impedance increase is artefactual, it is reproducible and constant across high frequencies, which could allow it to be used for EIT nerve imaging. Using high-frequency currents will allow accurate extraction of impedance changes even with high characteristic frequencies.

c) Does it differ from the previous modelling?

The active models developed in this study generally support findings obtained with the passive model created for the same purpose [16]. However, comparison of the active models demonstrated that the rate of the decrease with frequency may be different depending on the ion channels present in the membrane, which can be of high importance in choosing the optimal AC frequency for imaging the particular nerve with fast neural EIT. Also, the active models predict the existence of positive impedance changes at DC and high frequencies which are due to be experimentally validated.

3) Which model options are recommended for further modelling studies?

The models predicted similar general dependence of impedance on frequency, which matched experimental data (Fig. 6), apparent positive impedance changes on higher frequencies (Fig. 6), dependence of dZ on dimensions of the models (Fig. 7) and the same biophysical nature of the observed impedance changes (Fig. 10). However, there were also differences: the temporal and spatial properties of the action potentials (Fig. 3), the slope of the decrease of dZ with frequency (Fig. 6) and the maximum injected current not causing artefacts (Fig. 5).

Therefore, as distinctions exist, and because the C fibre model was experimentally validated on human nociceptors, it must be currently chosen over the HH model for inclusion to a full future model of the autonomic nerve. The paradigm used to build HH model with multiple axons (Fig. 11) could also be used.

C. Limitations and technical difficulties

The main technical problem faced during modelling was the lack of computational resources due to the highly nonlinear nature of the equations to be solved simultaneously on a large FEM mesh. For example, the complex C fibre model described in this study took about a day to compute at a single frequency on a 16-core workstation. Simulations of 3D HH models with multiple fibres also were very slow: the 8-axonal model took approximately 2 days to be computed. It may be expected to rise dramatically with the number of fibres and with added complex ion channels. To develop a full model, thousands of such interacting fibres are needed making the brute force approach to the project to be inadequate.

There are two possible ways to overcome this limitation. The first is to simplify the model so that it is calculated faster. This could be achieved by the development of a lumped bidomain model approach which was originally made to simulate cardiac tissue [48] but was also adapted for nerve bundles [32], [49], [50]. In this model, groups of fibres are treated as a uniformly distributed medium so that the membrane, extracellular and intracellular spaces occupy the same volume and are described by the same set of equations as any other model of a single fibre. However, the bidomain approach has several shortcomings: 1) it does not take into account the discrete fibre geometry which may become important when they possess different properties or fire non-synchronously [46]; 2) if external electrodes are used, while affecting fibres lying close to the nerve periphery, the membrane potential of the deeper fibres may not reach the threshold affecting the overall behaviour of the nerve [51]; 3) the fibres are usually not uniformly distributed in the nerve as bidomain model implies. To find out if these limitations are vital for our purpose, it would be desirable to study this model in future work.

The second approach to accelerate computations is the search for technical solutions to run the precise model with separate fibres more rapidly. These solutions may include the use of GPU acceleration or more efficient parallelizing involving the division of the model into several parts.

V. Conclusion

In this study, full 3D FEM models of single and multiple interacting nerve fibres were developed. The activity of the fibres was modelled using either the HH model of squid giant axon or the mammalian C fibre model. With these models, impedance changes during action potential propagation were simulated under various external conditions.

The simulated negative dZ were in agreement with available experimental data; and positive dZ at higher frequencies were predicted. The model allows for an optimized method of EIT for unmyelinated nerves by predicting the necessary parameters of the injected current and the optimal size and position of the electrodes. By studying membrane currents during EIT current injection, the model provided a biophysical explanation of the simulated impedance changes which is of high importance for understanding the nature of observed experimental results.

The developed model is a basis for a full model of the nerve, currently under development, which will additionally include myelinated fibres and interstitial space. The final model will have applications which include, but are not limited to, optimization of EIT for imaging in all kinds of nerves and study of the underlying causes of various nerve disorders.

References

[1] D. Holder, “Introduction to biomedical electrical impedance tomography,” in *Electrical Impedance Tomography: Methods, History and Applications*, London: IOP Publishing, 2004, pp. 423–451.

[2] T. Oh *et al.*, “A novel method for recording neuronal depolarization with recording at 125-825 Hz: Implications for imaging fast neural activity in the brain with electrical impedance tomography,” *Med. Biol. Eng. Comput.*, vol. 49, no. 5, pp. 593–604, 2011.

[3] K. Y. Aristovich *et al.*, “A method for reconstructing tomographic images of evoked neural activity with electrical impedance tomography using intracranial planar arrays,” *Physiol. Meas.*, vol. 35, no. 6, pp. 1095–109, 2014.

[4] Kristoffer Famm, “A jump-start for electroceuticals,” *Nature*, vol. 496, pp. 159–61, 2013.

[5] S. Baillet *et al.*, “Electromagnetic brain mapping,” *IEEE Signal Process. Mag.*, vol. 18, no. 6, pp. 14–30, 2001.

[6] T. D. Yoshida Kozai *et al.*, "Ultrasmall implantable composite microelectrodes with bioactive surfaces for chronic neural interfaces," *Nat. Mater.*, vol. 11, no. 12, pp. 1065–1073, Nov. 2012.

[7] E. M. C. Hillman, "Optical brain imaging in vivo: techniques and applications from animal to man," *J. Biomed. Opt.*, vol. 12, no. 5, p. 051402, 2007.

[8] V. Ntziachristos, "Going deeper than microscopy: the optical imaging frontier in biology," *Nat. Methods*, vol. 7, no. 8, pp. 603–614, Aug. 2010.

[9] K. Aristovich *et al.*, "Imaging fascicle traffic in peripheral nerve using fast neural EIT," in *Proceedings of the16th International Conference on Biomedical Applications of Electrical Impedance Tomography*, 2015, p. 75.

[10] R. H. Bayford, "BIOIMPEDANCE TOMOGRAPHY (ELECTRICAL IMPEDANCE TOMOGRAPHY)," *Annu. Rev. Biomed. Eng.*, vol. 8, no. 1, pp. 63–91, Aug. 2006.

[11] K. Y. Aristovich *et al.*, "Imaging fast electrical activity in the brain with electrical impedance tomography," *Neuroimage*, vol. 124, pp. 204–213, 2016.

[12] K. Y. Aristovich *et al.*, "Investigation of potential artefactual changes in measurements of impedance changes during evoked activity: implications to electrical impedance tomography of brain function.," *Physiol. Meas.*, vol. 36, no. 6, pp. 1245–59, 2015.

[13] D. S. Holder, "Impedance changes during the compound nerve action potential: Implications for impedance imaging of neuronal depolarisation in the brain," *Med. Biol. Eng. Comput.*, vol. 30, no. 2, pp. 140–146, Mar. 1992.

[14] K. G. Boone, "The possible use of applied potential tomography for imaging action potentials in the brain," University College London, 1995.

[15] O. Gilad *et al.*, "A method for recording resistance changes non-invasively during neuronal depolarization with a view to imaging brain activity with electrical impedance tomography," *J. Neurosci. Methods*, vol. 180, no. 1, pp. 87–96, 2009.

[16] A. Liston *et al.*, "A cable theory based biophysical model of resistance change in crab peripheral nerve and human cerebral cortex during neuronal depolarisation: implications for electrical impedance tomography of fast neural activity in the brain," *Med. Biol. Eng. Comput.*, vol. 50, no. 5, pp. 425–437, May 2012.

[17] M. Faulkner *et al.*, "Characterising the frequency response of impedance changes during evoked physiological activity in the rat brain," *Physiol. Meas.*, pp. 0–17, 2017.

[18] A. Vongerichten, "Imaging Physiological and Pathological Activity in the Brain using Electric Impedance Tomography," University College London, 2015.

[19] G. Schmidt, Robert F., Thews, "Fundamentals of Cell Physiology," in *Human Physiology*, 2nd ed., Berlin, Heidelberg: Springer Berlin Heidelberg, 1989, pp. 2–18.

[20] G. Schmidt, Robert F., Thews, "Information Transfer by Electrical Excitation," in *Human Physiology*, 2nd ed., Berlin, Heidelberg: Springer Berlin Heidelberg, 1989, pp. 19–42.

[21] A. L. Hodgkin and W. A. H. Rushton, "The Electrical Constants of a Crustacean Nerve Fibre," *Proc. R. Soc. B Biol. Sci.*, vol. 133, no. 873, pp. 444–479, Dec. 1946.

[22] D. Durand, "The somatic shunt cable model for neurons.," *Biophys. J.*, vol. 46, no. 5, pp. 645–53, 1984.

[23] P. J. Basser, "Cable equation for a myelinated axon derived from its microstructure," *Med. Biol. Eng. Comput.*, vol. 31, no. S1, pp. S87–S92, Jul. 1993.

[24] A. L. Hodgkin and A. F. Huxley, "A quantitative description of membrane current and its application to conduction and excitation in nerve," *J. Physiol.*, vol. 117, no. 4, pp. 500–544, Aug. 1952.

[25] D. R. Scriven, "Modeling repetitive firing and bursting in a small unmyelinated nerve fiber," *Biophys. J.*, vol. 35, no. 3, pp. 715–730, Sep. 1981.

[26] R. I. Herzog *et al.*, "Persistent TTX-resistant Na+ current affects resting potential and response to depolarization in simulated spinal sensory neurons.," *J. Neurophysiol.*, vol. 86, no. 3, pp. 1351–64, 2001.

[27] J. Tigerholm *et al.*, "Modeling activity-dependent changes of axonal spike conduction in primary afferent C-nociceptors.," *J. Neurophysiol.*, vol. 111, no. 9, pp. 1721–35, 2014.

[28] K. P. Cross and R. M. Robertson, "Ionic mechanisms maintaining action potential conduction velocity at high firing frequencies in an unmyelinated axon," *Physiol. Rep.*, vol. 4, no. 10, pp. 1–18, 2016.

[29] Jihwan Woo *et al.*, "Biophysical Model of an Auditory Nerve Fiber With a Novel Adaptation Component," *IEEE Trans. Biomed. Eng.*, vol. 56, no. 9, pp. 2177–2180, 2009.

[30] J. Howells *et al.*, "The voltage dependence of I h in human myelinated axons," *J. Physiol.*, vol. 590, no. 7, pp. 1625–1640, 2012.

[31] S. Qiao and K. Yoshida, "Influence of unit distance and conduction velocity on the spectra of extracellular action potentials recorded with intrafascicular electrodes," *Med. Eng. Phys.*, vol. 35, no. 1, pp. 116–124, 2013.

[32] S. Yin *et al.*, "Bidomain Modeling of Neural Tissue," in *Neural Engineering*, Boston, MA: Springer US, 2013, pp. 389–404.

[33] N. A. Pelot *et al.*, "Modeling the response of small myelinated axons in a compound nerve to kilohertz frequency signals," *J. Neural Eng.*, vol. 14, no. 4, p. 046022, Aug. 2017.

[34] P. L. Sheets *et al.*, "A Nav1.7 channel mutation associated with hereditary erythromelalgia contributes to neuronal hyperexcitability and displays reduced lidocaine sensitivity.," *J. Physiol.*, vol. 581, no. Pt 3, pp. 1019–31, 2007.

[35] T. Kiss, "Persistent Na-channels: Origin and function," *Acta Biol. Hung.*, vol. 59, no. Supplement 2, pp. 1–12, 2008.

[36] F. Maingret *et al.*, "Inflammatory mediators increase Nav1.9 current and excitability in nociceptors through a coincident detection mechanism.," *J. Gen. Physiol.*, vol. 131, no. 3, pp. 211–225, 2008.

[37] M. A. McAlexander and B. J. Undem, "Potassium channel blockade induces action potential generation in guinea-pig airway vagal afferent neurones," *J. Auton. Nerv. Syst.*, vol. 78, no. 2–3, pp. 158–164, 2000.

[38] E. Cooper, "Inactivation of A currents and A channels on rat nodose neurons in culture," *J. Gen. Physiol.*, vol. 94, no. 5, pp. 881–910, Nov. 1989.

[39] E. P. Christian and J. A. Togo, "Excitable properties and underlying Na+ and K+ currents in neurons from the guinea-pig jugular ganglion," *J. Auton. Nerv. Syst.*, vol. 56, no. 1–2, pp. 75–86, Dec. 1995.

[40] U. Bischoff *et al.*, "Na+-activated K+ channels in small dorsal root ganglion neurones of rat.," *J. Physiol.*, vol. 510 (Pt 3, pp. 743–754, 1998.

[41] A. Lüthi and D. A. McCormick, "H-current: Properties of a neuronal and network pacemaker," *Neuron*, vol. 21, no. 1, pp. 9–12, 1998.

[42] D. DiFrancesco *et al.*, "Properties of the hyperpolarizing-activated current (if) in cells isolated from the rabbit sino-atrial node.," *J. Physiol.*, vol. 377, no. 1, pp. 61–88, Aug. 1986.

[43] O. C. Zienkiewicz *et al.*, *The finite element method*. London: McGraw-hill, 1977.

[44] S. Elia and P. Lamberti, "The Reproduction of the Physiological Behaviour of the Axon of Nervous Cells by Means of Finite Element Models," in *Innovations in Intelligent Machines -3.Studies in Computational Intelligence*, Springer Berlin Heidelberg, 2013, pp. 69–87.

[45] K. S. Cole and H. J. Curtis, "Electric Impedance of the Squid Giant Axon During Activity.," *J. Gen. Physiol.*, vol. 22, no. 5, pp. 649–70, 1939.

[46] J. W. Clark and R. Plonsey, "Fiber Interaction in a Nerve Trunk," *Biophys. J.*, vol. 11, no. 3, pp. 281–294, Mar. 1971.

[47] R. C. Barr and R. Plonsey, "Electrophysiological interaction through the interstitial space between adjacent unmyelinated parallel fibers.," *Biophys. J.*, vol. 61, no. 5, pp. 1164–1175, 1992.

[48] W. T. Miller and D. B. Geselowitz, "Simulation studies of the electrocardiogram. I. The normal heart," *Circ. Res.*, vol. 43, no. 2, pp. 301–315, Aug. 1978.

[49] K. W. Altman and R. Plonsey, "Development of a model for point source electrical fibre bundle stimulation," *Med. Biol. Eng. Comput.*, vol. 26, no. 5, pp. 466–475, 1988.

[50] R. Sadleir, "A bidomain model for neural tissue," *Int J Bioelectromag*, vol. 12, no. 1, pp. 2–6, 2010.

[51] K. W. Altman and R. Plonsey, "Point source nerve bundle stimulation: Effects of fiber diameter and depth on simulated excitation," *IEEE Trans. Biomed. Eng.*, vol. 37, no. 7, pp. 688–698, 1990.